Bound and autoionizing potential energy curves in the CH molecule

Cite as: J. Chem. Phys. 159, 224111 (2023); doi: 10.1063/5.0177822 Submitted: 24 September 2023 • Accepted: 20 November 2023 • Published Online: 12 December 2023











Dávid Hvizdoš, 1,a) D Joshua Forer, 2,3 D Viatcheslav Kokoouline, 2 D and Chris H. Greene D





AFFILIATIONS

- Department of Physics and Astronomy and Purdue Quantum Science and Engineering Institute, Purdue University, West Lafayette, Indiana 47907, USA
- ²Department of Physics, University of Central Florida, Orlando, Florida 32816, USA
- Institut des Sciences Moléculaires, Université de Bordeaux, CNRS UMR 5255, 33405 Talence Cedex, France

ABSTRACT

This article presents a method of computing bound state potential curves and autoionizing curves using fixed-nuclei R-matrix data extracted from the Quantemol-N software suite. It is a method based on two related multichannel quantum-defect theory approaches. One is applying bound-state boundary conditions to closed-channel asymptotic solution matrices, and the other is searching for resonance positions via eigenphase shift analysis. We apply the method to the CH molecule to produce dense potential-curve datasets presented as graphs and supplied as tables in the publication supplement.

Published under an exclusive license by AIP Publishing. https://doi.org/10.1063/5.0177822

I. INTRODUCTION

The CH molecule and its positive ion CH+ play an important role in certain molecular plasma environments, such as in the interstellar medium or electric discharges and flames of hydrocarbon gases. The dominant process in the destruction of the CH⁺ ions in such environments is typically dissociative recombination (DR) with electrons: The ion recombines with an incident electron, forming a neutral molecule, typically in a highly excited electronic state of CH, and then the molecule dissociates. Our recent work1 was devoted to the process. It was found that the three lowest electronic states $(X^1\Sigma^+, a^3\Pi, \text{ and } A^1\Pi)$ of the CH⁺ ion contribute to the process: they produce low-energy resonances in the DR spectrum, increasing significantly the DR cross section. The presence of multiple low-energy excited states means that the resulting CH potential and autoionizing curves contain multiple crossing series of Rydberg states, which result in many complex avoided crossings. This study is devoted to the determination of highly excited electronic bound states of CH and autoionizing resonances.

Motivated, in particular, by the DR process, the lowest electronic states of the CH molecule have been studied in many theoretical and experimental studies. Here, we give a short overview of theoretical studies. As early as 1970, Liu and Verhaegen² used the LCAO-MO-SCF method and computed potential energy curves (PEC) as functions of the internuclear distance for nine low electronic states. Later, Bardsley and Junker,3 as well as Krauss and Julienne, 4 studied in more detail the energies of the CH electronic states near the equilibrium position and the energy of the ground state of the ion $(X^1\Sigma^+)$ in order to assess how fast the DR process is in CH⁺. They have used a method⁵ of mixed orbital sets composed of Slater-type orbitals and elliptic orbitals. In 1977, Giusti-Suzor and Lefebvre-Brion⁶ also performed calculations of several PECs at energies and geometries near the equilibrium of the ion, using the ion virtual orbital method of Lefebvre-Brion.⁷ For a photodissociation study, van Dishoeck8 determined PECs for more than a dozen electronic states of CH using a method of multireference configuration interaction (MRCI). Interestingly, knowing now quite well the CH and CH⁺ structure at low energies, we can notice that the region of energies near the CH+ equilibrium in the study by van Dishoeck⁸ was not computed as accurately as in earlier studies, such as by Giusti-Suzor and Lefebvre-Brion. Soon later, Takagi et al.,9 for a study on DR in CH+, computed several PECs using the ALCHEMY code based on the Slater-type orbitals, obtaining very accurate results, at least near the CH+ equilibrium. In 1999, Kalemos et al. 10 published PECs for more than a dozen CH electronic states obtained using the MRCI method and the Molpro suite of

a) Author to whom correspondence should be addressed: hvizdosdavid@gmail.com

codes. More recently, Vázquez *et al.*¹¹ have published very accurate PECs of the lowest states obtained with MRCI. The focus of that study was the 3*d* Rydberg states of CH, assigned previously to be responsible for two observed but unidentified interstellar bands. We mention here also spectroscopy-accurate coupled-cluster calculations by Shi *et al.*¹² of the PECs of the ground electronic state of CH. In a more recent calculation, Chakrabarti *et al.*¹³ employed the UK *R*-matrix code¹⁴ to produce a few PEC of the Rydberg states, as well as energies and widths of the lowest autoionizing states of CH. The approach employed in that study is very different from the quantum-chemistry approaches used in other studies mentioned earlier.

The theoretical approach presented here is very different from all the methods mentioned earlier, though it has some similarities to the one used by Chakrabarti et al. 13 It also employs the R-matrix formalism. It is more similar in spirit to the method used by Little and Tennyson¹⁵ in their calculations of PECs of N₂, which employs quantum defect theory 16,17 and certain elements of the scattering theory even for bound state calculations. There are advantages to working with the scattering information in the smoothest energyand internuclear-R-dependences possible, especially if a rovibrational frame transformation will ultimately be carried out, e.g., to determine inelastic scattering or rearrangement cross sections such as dissociative recombination.1 For this reason, we change from the R-matrix parameterization of the scattering data to a multichannel quantum defect theory (MQDT) representation (i.e., the K-matrix or its equivalent representation in terms of eigen quantum defects and eigenvectors) with comparatively smooth energy dependences. There is a slight cost in accuracy by doing this, namely the fact that by matching to Coulomb functions at the R-matrix boundary r_0 , we neglect the long range couplings at $r > r_0$. Our tests show that those couplings are rather small in practice and can be approximately treated perturbatively when higher accuracy is desirable.

Unless otherwise stated, we use atomic units throughout this article.

II. THEORETICAL OUTLINE

The main part of this method is applying asymptotic MQDT procedures to fixed-nuclei electron-scattering R matrix data. We obtain our $CH^+ + e^-$ electron-scattering R matrix by employing the Quantemol-N software suite, 18 which uses the UKRMol R-matrix method. The main output of this software is the energydependent reactance matrix K at a large electronic distance, with its elements representing physically open channels. The relevant quantum numbers of these channels are the electronic state of the target ion n, the orbital angular momentum l of the scattering electron, and its projection λ onto the molecular axis (though λ will not explicitly appear in our later derivations). For simplicity, let us combine these into a joint index $i = \{n_i, l_i, \lambda_i\}$. Let us also denote the channel threshold E_i and the channel energies $\varepsilon_i = E - E_i$, where E is some given total energy in Hartree energy units. It will also be useful to define the effective quantum number for closed channels

$$v_i = (-2\varepsilon_i)^{-1/2}. (1)$$

These Quantemol calculations employ the configuration-interaction method (CI). The correlation consistent polarized valence quadruple-zeta (cc-pVQZ) basis set was used to represent the electronic state of the target ion. In the CI expansion, the lowest orbital $1\sigma^2$ was frozen, while the remaining four electrons were distributed over the $2-7\sigma$, $1-3\pi$, and 1δ orbitals of the active space. Three σ and two π virtual orbitals were used to augment the continuum orbital set in the inner region scattering wave function. The three lowest target states, $X^1\Sigma^+$, $a^3\Pi$, and $A^1\Pi$, were retained in the closed-coupling expansion in the outer region. The orbital angular momentum of the scattered electron goes up to 4, and the R-matrix box radius r_0 was 13 bohr radii. The coordinate system places the CH $^+$ center of mass at its origin.

A. Extracting the R and K matrices

An important intermediate output of Quantemol is the fixed-nuclei R-matrix data. The program solves the Schrödinger equation inside a restricted electronic box with an arbitrary boundary condition. The solutions $|\psi_p\rangle$ are then projected onto physical outer-region channels $|i\rangle$ to get the surface amplitudes $w_{ip}=\langle\langle i|\psi_p\rangle\rangle$. The double angle bracket indicates that the integration is only carried out on the surface of a sphere of radius r_0 centered about the center of mass of the CH⁺ ion, as opposed to integration over all space. Note that these quantities are energy-independent, and at this point, it cannot be said whether an outer-region channel i is physically open or closed. The saved surface amplitudes w_{ip} along with the inner-solution R-matrix pole energies E_p can be plugged into the Wigner-Eisenbud²¹ formula to give the R matrix at an arbitrary energy,

$$R_{ii'} = \frac{1}{2} \sum_{p} \frac{w_{ip} \ w_{i'p}^*}{E_p - E}.$$
 (2)

The short-range R matrix obtained via Eq. (2) has indices of both open and closed channels. If we wish, we can transform it using a preliminary elimination procedure (closely related to the MQDT closed-channel elimination procedure), which neglects long-range multipole couplings at $r > r_0$,

$$\underline{R}^{\text{phys}} = \underline{R}_{oo} - \underline{R}_{oc} \left[\underline{R}_{cc} - \underline{W}_{c} \left(\underline{W}'_{c} \right)^{-1} \right]^{-1} \underline{R}_{co}, \tag{3}$$

where o and c denote blocks of open and closed channels, respectively, and W_c is a diagonal matrix of the asymptotically decaying (for negative energies) Whittaker functions evaluated at the closed-channel energies using the R-matrix box radius and the respective electronic angular momenta. W_c' is its derivative with respect to the electronic coordinate. In our derivation, we use the "energy-normalized" Whittaker functions, ¹⁷ but the division W_c/W_c' makes re-scaling by any r-independent constant irrelevant in implementation. We can select which closed channels we eliminate this way (e.g., we can keep weakly closed channels while eliminating the strongly closed ones). For the derivation of this formula, see Appendix A. A note for readers less familiar with MQDT: this elimination of channels does not mean erasing physical information but merely decreasing the dimension of the R matrix by applying asymptotic boundary conditions.

Upon obtaining the R matrix, we transform it into the K matrix using the well-known relation 17

$$\underline{K} = (f - f'\underline{R})(g - g'\underline{R})^{-1},\tag{4}$$

where \underline{f} and \underline{g} are diagonal matrices of the regular and irregular Coulomb functions $f(\varepsilon_i, l_i, r_0)$, $g(\varepsilon_i, l_i, r_0)$. Primed quantities here and throughout denote an element-wise derivative with respect to the electronic coordinate, r. The pair $\{f,g\}$ is equal to the pair $\{s,-c\}$ in Seaton's work. These functions are well defined for all open channels and for weakly closed channels as long as $\varepsilon_i > -1/(2l_i^2)$. For lower energies, the functions become complex. Therefore, for closed channels with high l values ($l \ge 2$) that we do not eliminate, we replaced the pair $\{f,g\}$ with the rescaled $\{f^\eta,g^\eta\}$,

$$f^{\eta}(\varepsilon, l, r) = f(\varepsilon, l, r) / \sqrt{A(\varepsilon, l)},$$
 (5)

$$g^{\eta}(\varepsilon, l, r) = g(\varepsilon, l, r) \sqrt{A(\varepsilon, l)},$$
 (6)

where $A(\varepsilon, l) = \prod_{j=0}^{l} (1 + 2j^2 \varepsilon)$. This alternate pair has also been used in previous works, ^{22,23} though often rescaled by a factor of $\sqrt{2}$. This choice removes the complex behavior at negative energies but also alters some of the equations in the following sections.

The final step before branching into either the potential curve or autoionizing curve calculation is diagonalizing the *K* matrix,

$$K_{ii'} = \sum_{\rho} U_{i\rho} \tan(\tau_{\rho}) U_{i'\rho}^*,$$
 (7)

to obtain the eigenphase shifts τ_{ρ} and the unitary (real and orthogonal in this case) matrix $U_{i\rho}$. The two energy dependent objects contain all the main information necessary for finding the potential curves and autoionizing states.

The ability to evaluate Eq. (2) without the need to solve the Schrödinger equation again for each input energy is a key advantage of this approach. Eliminating the strongly closed channels while retaining the weakly closed ones in Eq. (3) is another key choice that gets rid of the more problematic channels that would otherwise hamper the evaluation of Eq. (4) while keeping the energy dependence of the resulting K matrix smoother than with a full elimination. Keeping some channels artificially open is also necessary for computing the potential curves below the lowest CH^+ target energy, where all channels are closed.

B. Bound-state curve calculation

This part of the approach is analogous to the multichannel spectroscopy treatment of bound-state energies by Aymar *et al.*¹⁷ (Subsection II D 2 in the reference).

In this case, we are looking at energies below the lowest target threshold where all channels are closed and, therefore, we can only eliminate a strict subset of them. As noted earlier, we eliminate only the strongly closed channels because eliminating fewer channels introduces less energy dependence into the K matrix and its related quantities. Using the eigenphase shifts and their

corresponding eigenvectors from Eq. (7), we can construct two new matrices.

$$\mathscr{S}_{ii'} = \sum_{\rho} U_{i\rho} \sin(\tau_{\rho}) U_{i'\rho}^{*}, \tag{8}$$

$$\mathscr{C}_{ii'} = \sum_{\rho} U_{i\rho} \cos(\tau_{\rho}) U_{i'\rho}^{*}, \tag{9}$$

which can be seen as the coefficients of a unitary transformation of the standard real-valued asymptotic solution matrix $\psi_{ii'}$,

$$\psi_{ii'} = f_i \delta_{ii'} - g_i K_{ii'},$$

$$\downarrow \qquad (10)$$

$$\tilde{\psi}_{ii'} = f_i \mathcal{C}_{ii'} - g_i \mathcal{S}_{ii'}.$$

They are to \underline{K} what sine and cosine are to the tangent function.

Let us now write the Coulomb functions in terms of the energy normalized Whittaker functions

$$f_i = -W_i \cos \beta_i + \bar{W}_i \sin \beta_i, \tag{11}$$

$$g_i = -W_i \sin \beta_i - \bar{W}_i \cos \beta_i, \tag{12}$$

where $\beta_i = \pi(v_i - l_i)$. Finding bound states means finding linear combinations of $\tilde{\psi}_{ii'}$ such that the exponentially rising part is removed (when there are open channels, this exists for any energy). Using Eqs. (10)–(12), it can be seen that the bound-state energies can be found wherever the matrix

$$\underline{D} = \mathcal{L} \cos(\beta) + \mathcal{C} \sin(\beta), \tag{13}$$

is singular. Remembering that we sometimes replace $\{f,g\}$ with the rescaled $\{f^{\eta},g^{\eta}\}$, we need to adjust this to

$$\underline{\tilde{D}} = \mathcal{L} \cos(\beta) + \mathcal{L} \sin(\beta)q^{-1}, \tag{14}$$

where the matrix \underline{q} is diagonal. Its elements are equal to 1 for channels that use $\{f, g\}$ and equal to $A(\varepsilon_i, l_i)$ for channels that use $\{f^{\eta}, g^{\eta}\}$. Altogether, finding the potential curves is equivalent to finding the roots of the determinant

$$\left|\underline{\tilde{D}}\right| = 0,\tag{15}$$

with respect to energy for each fixed-nuclei calculation. The advantage of going from the K matrix to $\mathscr S$ and $\mathscr C$ is that $\mathscr S$ and $\mathscr C$ do not have divergences and are, therefore, easier to work with numerically.

C. Autoionizing curve calculation

In the energy region between the target ground state and excited states lie the autoionizing curves. Their positions and widths are determined by the energy dependence of the eigenphase sum $\sum_{\rho} \tau_{\rho}(E)$ obtained from Eq. (7) (see Subsection II D 3 of Aymar *et al.*¹⁷). The resonance positions are at the peaks of the eigenphase sum energy derivative, and the full widths at half maximum are defined by

$$\Gamma = \frac{2}{\sum_{\rho} \frac{d\tau_{\rho}}{dE}\Big|_{E_{\text{peak}}}}.$$
 (16)

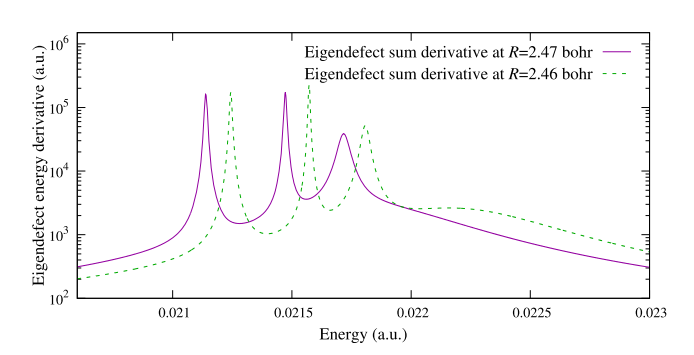


FIG. 1. The energy derivative of the eigenphase sum at two inter-nuclear distances (for the ${}^2\Sigma^+$ symmetry, zoomed-in to a particular energy window). The widest peak visible at R=2.46 bohr passes underneath the three narrow peaks at R=2.47 bohr.

For this method to correctly determine the physical autoionization widths, it is necessary to eliminate all the closed channels before computing the eigenphase shifts. This leads to a sharper energy behavior of the *K* matrix compared to the method from Sec. II B, so in practice we must sample a denser energy grid. A possible issue with this method is that peaks connected to wide resonances can sometimes be obfuscated in regions where they strongly overlap other narrower resonances. An example of this can be seen in Fig. 1.

A simpler, but less exact, alternative to this approach is to again keep some of the closed channels open when computing the K matrix, then cross out all the open channels and treat the remaining closed part with the procedure from Subsection II B. This simplified method neglects some of the channel couplings and does not allow determination of the resonance widths, but is useful as an approximation of the autoionizing curves because the resulting energies are usually very close to the ones obtained via the full approach (typically within one autoionization width Γ).

D. Separating symmetries of the molecule

The Quantemol software separates the problem into irreducible representations of the C_{2v} point group, namely A_1 , A_2 , B_1 , and B_2 . Hence, the R matrix is block diagonal with respect to these. After a simple unitary transformation of the R matrix, these blocks separate further into the actual physical symmetries of the problem. The transformation in question is connected to going from real-valued spherical harmonics to complex-valued ones and is described briefly in our previous publication. 1 A_1 gives us $^2\Sigma^+$ and $^2\Delta$, A_2 gives $^2\Sigma^-$ and $^2\Delta$ (identical to A_1), B_1 gives $^2\Pi$ and $^2\Phi$, and B_2 holds the same information as B_1 .

III. RESULTS AND DISCUSSION

Because a Rydberg series gets infinitely dense in energy as it approaches the threshold, we cut off our calculations at 0.15 eV below each threshold. The $^2\Sigma^+$ symmetry curves are in Figs. 2–5. Figure 2 shows the overall structure over the full breadth of computed energies. Figure 3 zooms in to energies closer to the ionic potential minimum. The structure is mostly dominated by a dense series of curves parallel to the closest target state energetically above (the ground state for the potential curves and the first excited state

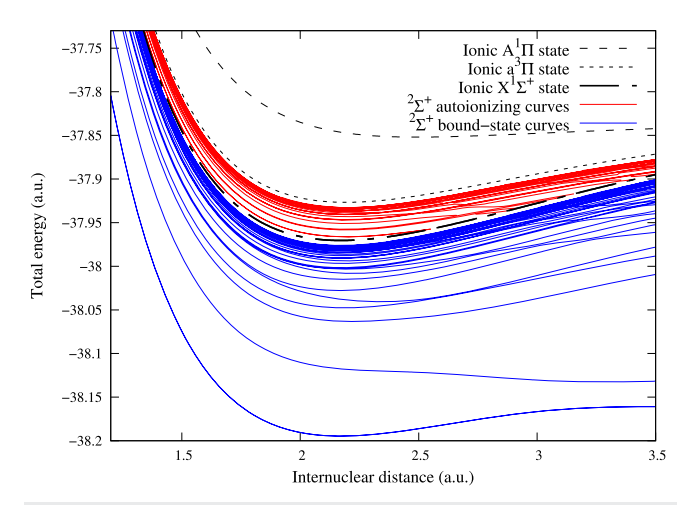


FIG. 2. The full breadth of the $^2\Sigma^+$ symmetry curves of CH. The thick dashed curves are the CH $^+$ target states. The autoionizing curves are the continuous red curves between the ground target state and the first excited target state. The bound-state curves are the continuous blue curves below the ground target state.

for the autoionizing curves), which are "cut through" by a sparser series of plunging resonances. This creates many series of avoided crossings and is most apparent from Figs. 4 and 5, which show the curves relative to the ground state energy. Figure 5 exchanges energy for the effective quantum number ν (with respect to the ground state), which demonstrates how the majority of the potential curves are placed at integer ν positions (as expected of a Rydberg series).

The remaining symmetries mostly feature similar behavior to that of ${}^2\Sigma^+$. The ${}^2\Sigma^-$ symmetry potential curves are in Fig. 6. All the ${}^2\Sigma^-$ symmetry channels are connected to excited electronic states of the target and, therefore, accumulate under a higher threshold and don't feature any autoionizing curves in the studied energy regions.

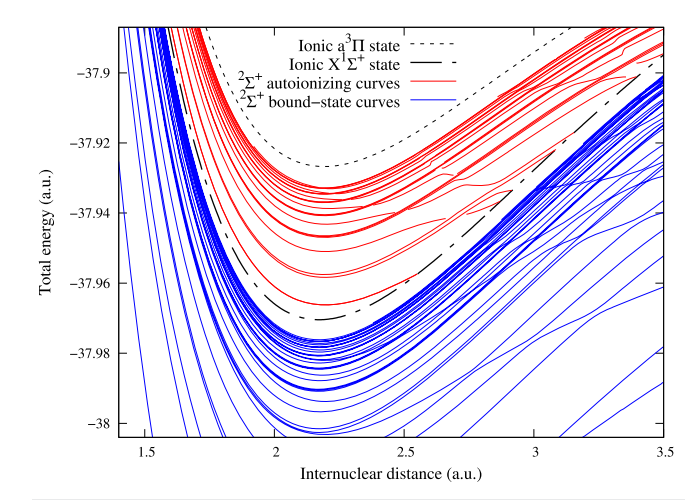


FIG. 3. The $^2\Sigma^+$ symmetry curves zoomed in. The dashed curves are CH⁺ target states. The continuous curves above $X^1\Sigma^+$ are autoionizing curves, and the ones below are bound-state curves.

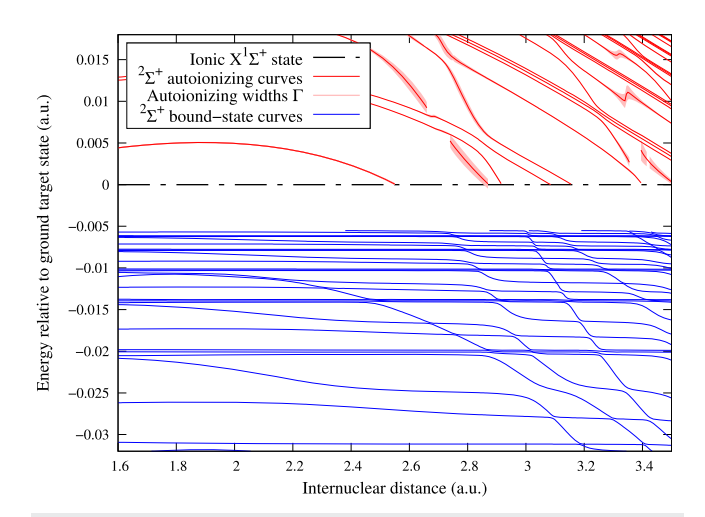


FIG. 4. The $^2\Sigma^+$ symmetry curves relative to the ground target state energy (zoomed in to energies close to the threshold). The autoionizing curves above the threshold now also have a shaded area denoting curve widths.

The $^{2}\Pi$ symmetry curves are in Fig. 7 and feature some of the densest crossing structures. Figure 8 shows a closeup of one of the avoided crossings, including the computed widths Γ . It demonstrates how the largest width diabatically crosses through the curves. Often, though, these crossings are where we lose data points because the widest curve is often completely hidden behind the band of narrow curves. Figure 9 shows a comparison with two previous calculations by Takagi et al.9 and Chakrabarti et al.13 It shows the so-called $2^2\Pi$ curve, which is the lowest curve that cuts through the Rydberg series, accumulating below $X^1\Sigma^+$. This curve is the continuation of the resonance, which crosses $X^1\Sigma^+$ closest to its minimum. As such, it is the most relevant resonance to direct dissociative recombination computations such as those of Amitay et al.²⁴ In our computations, the autoionizing curve cuts through $X^1\Sigma^+$ at 1.7 bohr. Do note that the compared curves have been digitized and interpolated from the aforementioned articles, and in the case of

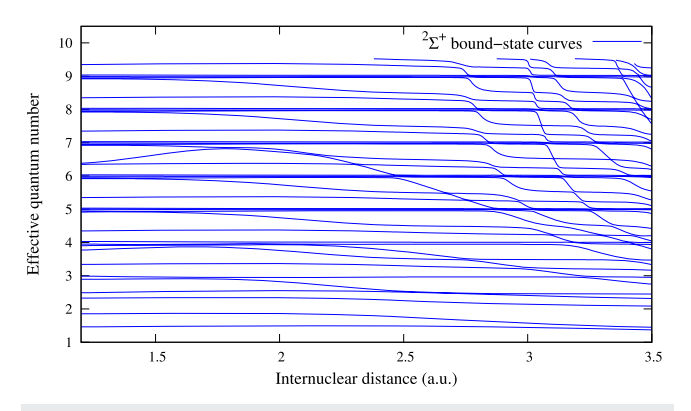


FIG. 5. The $^2\Sigma^+$ symmetry bound-state curve effective quantum number (compared to the ground target state).

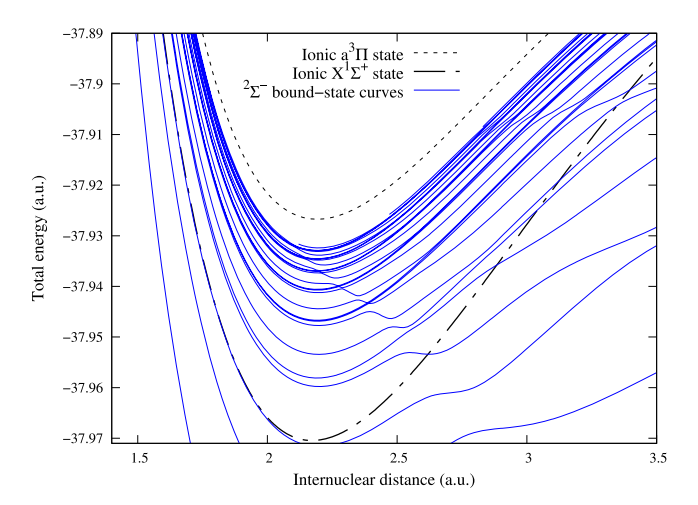


FIG. 6. The $^2\Sigma^-$ symmetry potential curves. The dashed curves are CH⁺ target states. All the continuous curves in this image are bound-state curves.

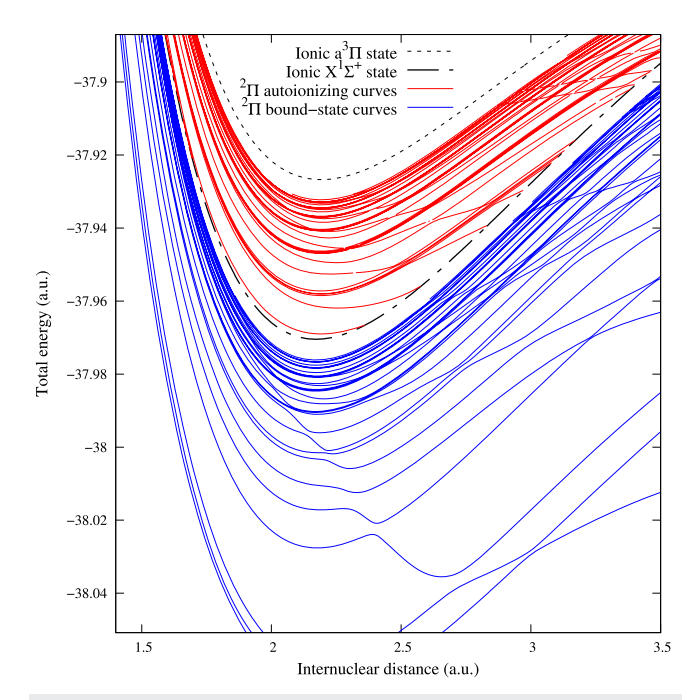


FIG. 7. The $^2\Pi$ symmetry curves. The dashed curves are CH⁺ target states. The continuous curves above X¹ Σ^+ are autoionizing curves, and the ones below are bound-state curves.

Chakrabarti *et al.*, the said curve only has four data points in the region from 2 to 2.5 bohr.

The $^2\Delta$ symmetry potential curves are in Fig. 10. The $^2\Phi$ symmetry potential curves, on the other hand, are almost exclusively at integer ν energies (relative to either the ground or first excited target state); they are in Fig. 11.

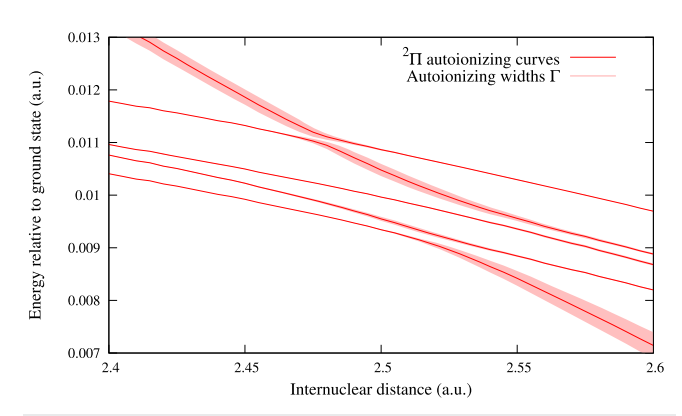


FIG. 8. A closeup of a $^2\Pi$ symmetry autoionizing curve avoided crossing featuring the curve widths with shaded areas.

A. Numerical limitations

In general, the widths of autoionizing curves are proportional to the Rydberg spacing 25

$$\Gamma(\varepsilon) \propto \frac{\mathrm{d}\varepsilon}{\mathrm{d}\nu}(\varepsilon) = \frac{1}{\nu^3(\varepsilon)},$$
 (17)

where ε is computed relative to the threshold that makes up the dominant channels of a given curve. The actual curve widths can vary significantly around the avoided crossings but within simpler regions (e.g., at internuclear distances less than 2 bohr for $^2\Sigma^+$) this scaling rule is mostly followed. If we compute the ratios $\Gamma_{\rm curve} v^3(\varepsilon_{\rm curve})$ for all the curves, they form tight bands with a variance of ~5%–15%. In practice, this scaling means that one should sample the energy grid with equidistant ν (relative to the closest higher threshold). For our specific computational setup, this means that the widths that are narrower than

$$\Gamma_{\text{limit}}(\varepsilon) = \frac{8.639 \times 10^{-4}}{v^3(\varepsilon)} \text{a.u.}, \tag{18}$$

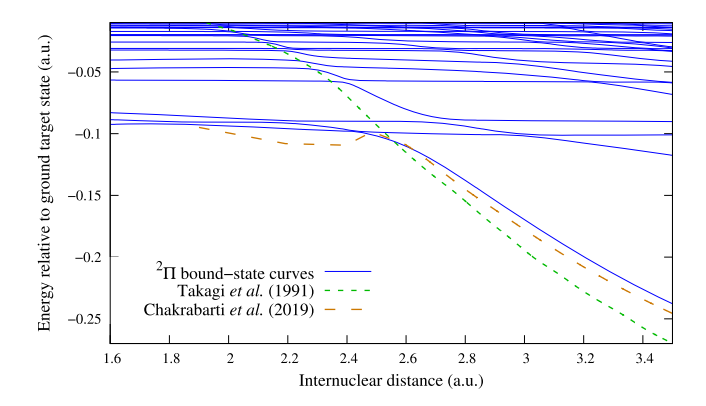


FIG. 9. A comparison of the $2^2\Pi$ curve from previous publications by Takagi *et al.*⁹ and Chakrabarti *et al.*¹³ The continuous curves are our computed bound-state curves, and the dashed curves are interpolated from the figures in the aforementioned publications.

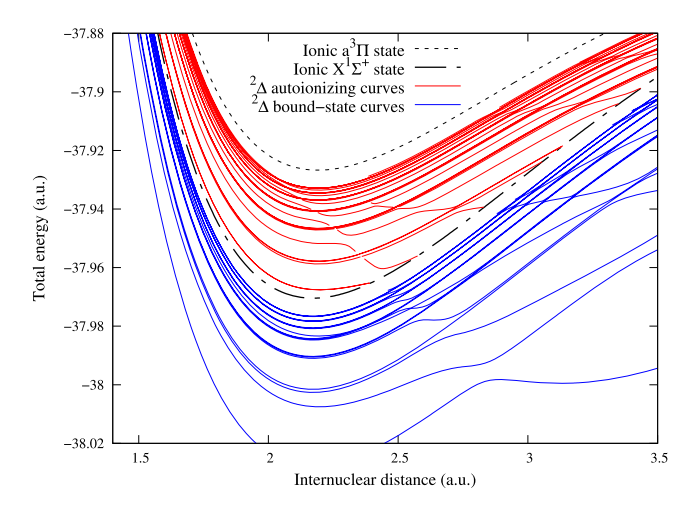


FIG. 10. The $^2\Delta$ symmetry curves. The dashed curves are CH+ target states. The continuous curves above X¹ Σ^+ are autoionizing curves, and the ones below are bound-state curves.

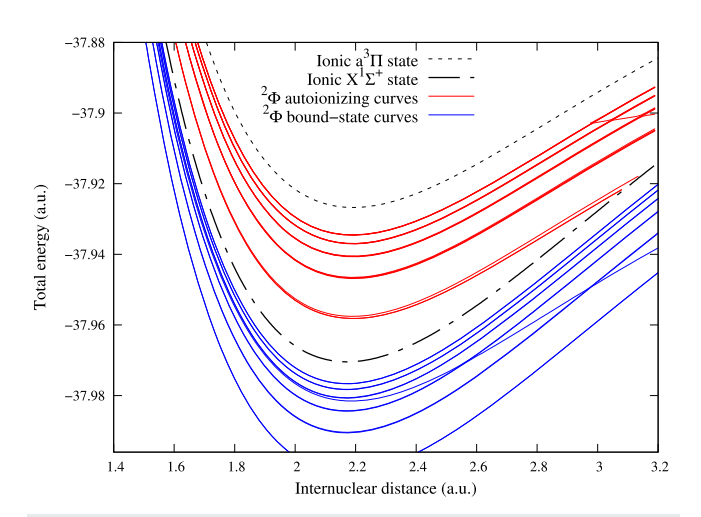


FIG. 11. The ${}^2\Phi$ symmetry curves. The dashed curves are CH+ target states. The continuous curves above $X^1\Sigma^+$ are autoionizing curves, and the ones below are bound-state curves.

start becoming unreliable, and curves with significantly lower widths are likely to be lost (ε is again relative to the closest higher threshold). In particular, the $^2\Phi$ symmetry is almost completely made up of curves that skirt this boundary.

IV. CONCLUSIONS

We have processed fixed-nuclei *R* matrix data from Quantemol using two methods to obtain bound-state curves and autoionizing curves in the energy region around the $X^1\Sigma^+$ state of CH^+ . The computations were performed for five symmetries of the molecule: ${}^2\Sigma^+$, ${}^2\Sigma^-$, ${}^2\Pi$, ${}^2\Delta$, and ${}^2\Phi$. The autoionizing curve data also features computed autoionizing widths.

SUPPLEMENTARY MATERIAL

The supplement to this article contains data files for all the curves shown in Figs. 2–11 (apart from the two curves extracted from previous studies in Fig. 9). The files are separated by symmetry and further separated into autoionizing curve files and bound-state curve files. All values are in atomic units.

In all of the files, the first column contains the internuclear distance, and the second, third, and fourth columns contain the $X^1\Sigma^+,$ $a^3\Pi,$ and $A^1\Pi$ energies, respectively. For the autoionizing curves, the following columns come in pairs containing a curve's energy relative to $X^1\Sigma^+$ followed by its width $\Gamma.$ The $^2\Phi$ symmetry autoionizing curve file does not contain widths due to insufficient resolution. The bound-state curve files also don't contain any widths. In cases where the data for a curve does not exist at a specific geometry (either because it isn't in the studied energy range or because it was temporarily lost in an avoided crossing as described in Fig. 1), the data entry at that position is a "?" symbol. The set of geometries used is the same for all files.

ACKNOWLEDGMENTS

We wish to acknowledge support from the National Science Foundation, Grant Nos. 2110279 (UCF) and 2102187 (Purdue).

AUTHOR DECLARATIONS

Conflict of Interest

The authors have no conflicts to disclose.

Author Contributions

Dávid Hvizdoš: Data curation (lead); Formal analysis (equal); Investigation (equal); Methodology (equal); Software (lead); Validation (equal); Visualization (lead); Writing - original draft (lead); Writing - review & editing (equal). Joshua Forer: Formal analysis (equal); Investigation (equal); Methodology (equal); Software (supporting); Validation (equal); Visualization (supporting); Writing – original draft (supporting); Writing – review & editing (equal). Viatcheslav Kokoouline: Conceptualization (equal); Formal analysis (equal); Funding acquisition (equal); Investigation (equal); Methodology (equal); Project administration (equal); Resources (equal); Software (supporting); Supervision (equal); Validation (equal); Visualization (supporting); Writing - original draft (supporting); Writing - review & editing (equal). Chris H. Greene: Conceptualization (equal); Data curation (supporting); Formal analysis (equal); Funding acquisition (equal); Investigation (equal); Methodology (equal); Project administration (equal); Resources (equal); Software (supporting); Supervision (equal); Validation (equal); Visualization (supporting); Writing - original draft (supporting); Writing – review & editing (equal).

DATA AVAILABILITY

The data that support the findings of this study are available within the article and its supplementary material.

APPENDIX A: R-MATRIX PRELIMINARY CHANNEL ELIMINATION

Because *R*-matrix channel elimination is not very common, we find it useful to write up our derivation for the formula (3). The ideas used here are similar to Gregory Breit's reduced *R*-matrix treatment²⁶ (Sec. 31 in the reference). We call this a preliminary elimination because in our frame transformation treatments, we use it to eliminate only the strongly closed channels in order to obtain a smooth fixed-nuclei *K* matrix, and it is the rovibrationally frame transformed *K* matrix that undergoes the full MQDT closed-channel elimination.

As a first step, recall that Eq. (4) can be derived from the definition of the R matrix as an inverse logarithmic derivative of a wave function. Let ψ_{iy} be the ith channel of the yth independent solution of the Schrödinger equation. In matrix formalism, one can write

$$\underline{R} = \underline{\psi}(\underline{\psi}')^{-1}\Big|_{r_0},\tag{A1}$$

where r_0 is the *R*-matrix box radius. This equation is valid for any choice of independent solutions. This means that for $r > r_0$, we can substitute the standard Coulomb functions $\{f,g\}$ and the matrix \underline{K} with an arbitrary pair of solutions to the radial Schrödinger equation $\{\tilde{f},\tilde{g}\}$ and their corresponding combination matrix \tilde{K} , i.e.,

$$\psi(r) = \tilde{f} - \tilde{g}\frac{\tilde{K}}{\tilde{K}}, \quad \text{for } r \ge r_0.$$
 (A2)

If we choose a pair that satisfies the conditions on the *R*-matrix box boundary,

$$\tilde{f}(\varepsilon, l, r_0) = 0, \qquad \tilde{f}'(\varepsilon, l, r_0) = 1,
\tilde{g}(\varepsilon, l, r_0) = 1, \qquad \tilde{g}'(\varepsilon, l, r_0) = 0,$$
(A3)

then Eq. (4) becomes $\underline{\tilde{K}} = -\underline{R}$ (at $r = r_0$). This means that we can also view the R matrix as a K matrix. Let us specifically choose the set of Coulomb functions

$$\tilde{f}(r) = -\frac{\pi}{2} [W(r)\bar{W}(r_0) - \bar{W}(r)W(r_0)],
\tilde{f}'(r) = -\frac{\pi}{2} [W'(r)\bar{W}(r_0) - \bar{W}'(r)W(r_0)],
\tilde{g}(r) = \frac{\pi}{2} [W(r)\bar{W}'(r_0) - \bar{W}(r)W'(r_0)],
\tilde{g}'(r) = \frac{\pi}{2} [W'(r)\bar{W}'(r_0) - \bar{W}'(r)W'(r_0)],$$
(A4)

where W and \bar{W} are a pair of "energy normalized" Whittaker functions, 17 with W exponentially decaying for closed channels and \bar{W} exponentially increasing. The ε and l arguments are omitted for brevity

Keeping with the standard MQDT closed-channel elimination procedure,¹⁷ we first partition the solution matrix into open and closed blocks,

$$\underline{\psi} = \begin{pmatrix} \underline{\psi_{oo}} & \underline{\psi_{oc}} \\ \underline{\psi_{co}} & \underline{\psi_{cc}} \end{pmatrix}, \tag{A5}$$

and then look for a linear combination matrix \underline{B} that kills off the exponentially rising behavior in the closed channels,

$$\underline{\psi}^{\text{phys}} = \underline{\psi} \left(\underline{\underline{B_{oo}}} \right) \to \begin{pmatrix} [\tilde{f}_o - \tilde{g}_o \tilde{K}_{oo}] \underline{B_{oo}} + [-\tilde{g}_o \tilde{K}_{oc}] \underline{B_{co}} \\ [-\tilde{g}_c \tilde{K}_{co}] \underline{B_{oo}} + [\tilde{f}_c - \tilde{g}_c \tilde{K}_{cc}] \underline{B_{co}} \end{pmatrix}. \tag{A6}$$

Combining Eqs. (A4) and (A6) while requiring that coefficients in front of \bar{W} be zero in all closed channels and evaluating at $r = r_0$ yields

$$\underline{B_{co}} = \left(\underline{W_c}(r_0) + \underline{W_c'}(r_0)\underline{\tilde{K}_{cc}}\right)^{-1} \left(-\underline{W_c'}(r_0)\underline{\tilde{K}_{co}}\right)\underline{B_{oo}}.$$
 (A7)

Setting the arbitrary B_{oo} equal to the identity matrix and substituting it into the open part of Eq. (A6), $\underline{\tilde{K}} = -\underline{R}$, then gives us

$$\underline{R}^{\text{phys}} = \underline{R_{oo}} - \underline{R_{oc}} \left(\underline{R_{cc}} - \underline{W_c} \left[\underline{W_c'} \right]^{-1} \right)^{-1} \underline{R_{co}}. \tag{A8}$$

Note here that an r-independent normalization of W does not change this equation.

APPENDIX B: ADDITIONAL CURVE PROPERTIES

If we artificially open all the channels in our *K* matrix connected to the first excited threshold and still implement the autoionizing curve procedure, we will get an approximate diabatization of the plunging resonances connected to the higher threshold, as shown in Fig. 12.

Another property of fixed-nuclei R-matrix data is that the lowest-lying bound-state curves coincide with the lowest-lying R matrix poles. This is shown in Fig. 13. The one set of poles that does not coincide with any curve shown instead coincides with the lowest curve in the $^2\Delta$ symmetry.

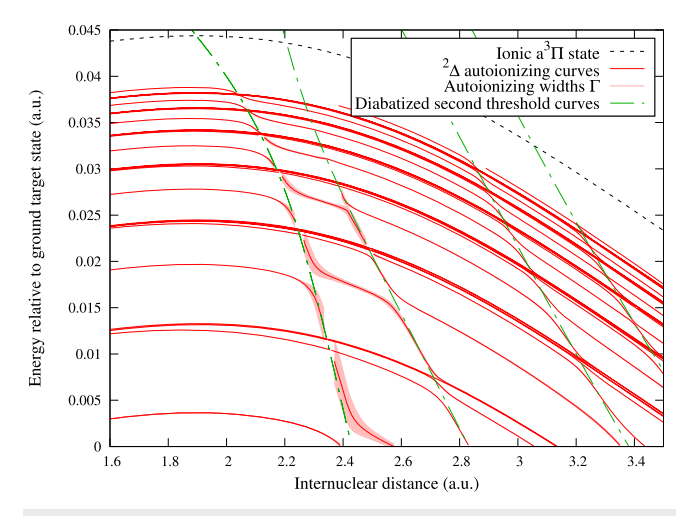


FIG. 12. The $^2\Delta$ symmetry autoionizing curves (continuous red curves with shaded width) compared to diabatized curves (dot–dashed green curves).

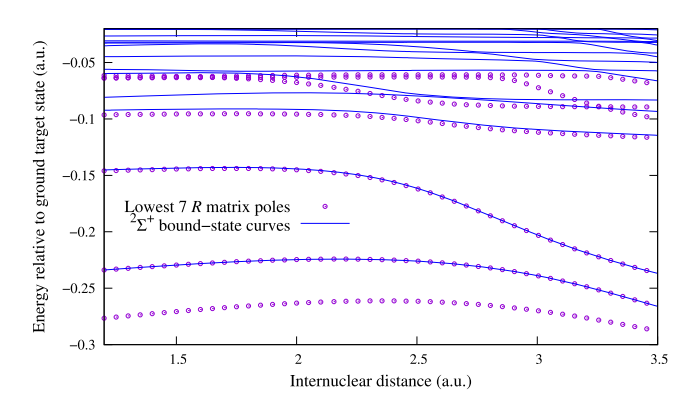


FIG. 13. The $^2\Sigma^+$ symmetry bound-state curves relative to the ground target state energy showing that the lowest curves coincide with the low *R*-matrix poles.

REFERENCES

(2007).

 $^1\mathrm{J}$ J. Forer, D. Hvizdoš, X. Jiang, M. Ayouz, C. H. Greene, and V. Kokoouline, "Unified treatment of resonant and nonresonant mechanisms in dissociative recombination: Benchmark study of CH+," Phys. Rev. A $\bf 107$, 042801 (2023).

²H. Liu and G. Verhaegen, "Electronic states of CH and NH," J. Chem. Phys. 53, 735–745 (1970).

³J. Bardsley and B. Junker, "Dissociative recombination of CH⁺ ions," Astrophys. J. **183**, L135 (1973).

⁴M. Krauss and P. S. Julienne, "Dissociative recombination of e+ CH⁺($^{1}\Sigma^{+}$)," Astrophys. J. **183**, L139 (1973).

⁵J. C. Browne and F. A. Matsen, "Quantum-mechanical calculations for the electric field gradients and other electronic properties of lithium hydride: The use of mixed orbital sets." Phys. Rev. 135, A1227–A1232 (1964).

 6 A. Giusti-Suzor and H. Lefebvre-Brion, "The dissociative recombination of CH+ ions," Astrophys. J. **214**, L101–L103 (1977).

⁷H. Lefebvre-Brion, "On the calculation of rydberg states of some diatomic molecules," J. Mol. Struct. 19, 103–107 (1973).

⁸E. F. van Dishoeck, "Photodissociation processes in the CH molecule," J. Chem. Phys. **86**, 196–214 (1987).

⁹H. Takagi, N. Kosugi, and M. L. Dourneuf, "Dissociative recombination of CH⁺," J. Phys. B. At., Mol. Opt. Phys. **24**, 711 (1991).

¹⁰ A. Kalemos, A. Mavridis, and A. Metropoulos, "An accurate description of the

ground and excited states of CH," J. Chem. Phys. 111, 9536–9548 (1999).

11G. Vázquez, J. Amero, H. Liebermann, R. Buenker, and H. Lefebvre-Brion, "Insight into the Rydberg states of CH," J. Chem. Phys. 126, 164302 (2007).

 12 D.-H. Shi, J.-P. Zhang, J.-F. Sun, Y.-F. Liu, Z.-L. Zhu, and B.-H. Yu, "Accurate analytic potential energy function and spectroscopic study for CH (X $^2\Pi$) radical using coupled-cluster theory in combination with the correlation-consistent

quintuple basis set," J. Mol. Struct.: THEOCHEM **860**, 101–105 (2008). ¹³K. Chakrabarti, R. Ghosh, and B. Choudhury, "R-matrix calculation of bound and continuum states of CH," J. Phys. B: At., Mol. Opt. Phys. **52**, 105205 (2019).

¹⁴J. Tennyson, "Electron-molecule collision calculations using the R-matrix method," Phys. Rep. 491, 29–76 (2010).

¹⁵D. A. Little and J. Tennyson, "An ab initio study of singlet and triplet Rydberg states of N₂," J. Phys. B: At., Mol. Opt. Phys. 46, 145102 (2013).

¹⁶M. J. Seaton, "Coulomb functions for attractive and repulsive potentials and for

positive and negative energies," Comput. Phys. Commun. 146, 225–249 (2002). ¹⁷M. Aymar, C. H. Greene, and E. Luc-Koenig, "Multichannel Rydberg spectroscopy of complex atoms," Rev. Mod. Phys. 68, 1015–1123 (1996).

N. Vinci, "Quantemol-N: An expert system for performing electron molecule collision calculations using the R-matrix method," J. Phys.: Conf. Ser. 86, 012001

26 July 2024 20:15:47

- ¹⁹ J. M. Carr, P. G. Galiatsatos, J. D. Gorfinkiel, A. G. Harvey, M. A. Lysaght, D. Madden, Z. Mašín, M. Plummer, J. Tennyson, and H. N. Varambhia, "UKRmol: A low-energy electron- and positron-molecule scattering suite," Eur. Phys. J. D 66, 58 (2012).
- ²⁰ J. Tennyson and C. J. Noble, "RESON—A program for the detection and fitting of Breit-Wigner resonances," Comput. Phys. Commun. 33, 421–424 (1984).
- ²¹E. P. Wigner and L. Eisenbud, "Higher angular momenta and long range interaction in resonance reactions," Phys. Rev. 72, 29–41 (1947).
- ²²C. Greene, U. Fano, and G. Strinati, "General form of the quantum-defect theory," Phys. Rev. A 19, 1485–1509 (1979).
- 23 S. Bezzaouia, M. Telmini, and C. Jungen, "Variational *R*-matrix calculations for singly and doubly excited singlet gerade channels in H₂," Phys. Rev. A **70**, 012713 (2004).
- ²⁴Z. Amitay, D. Zajfman, P. Forck, U. Hechtfischer, B. Seidel, M. Grieser, D. Habs, R. Repnow, D. Schwalm, and A. Wolf, "Dissociative recombination of CH⁺: Cross section and final states," Phys. Rev. A 54, 4032–4050 (1996).
- ²⁵U. Fano and A. R. P. Rau, Atomic Collisions and Spectra (Academic Press, Orlando, FL, 1986).
- ²⁶G. Breit, "Theory of resonance reactions and allied topics," in *Nuclear Reactions II: Theory/Kernreaktionen II: Theorie* (Springer, Berlin, Heidelberg, 1959), pp. 1–407.